Solidification of Metallic Alloys: Does the Structure of the Liquid Matter?

M. RAPPAZ, PH. JARRY, G. KURTULDU, and J. ZOLLINGER

In 1952, Frank (Proc R Soc Lond Ser-Math Phys Sci 215:43–46, 1952) already postulated that Icosahedral Short Range Order (ISRO) of atoms in the liquid could possibly explain the large nucleation undercoolings measured in metallic alloys by Turnbull and Fisher (J Chem Phys 17:71–73, 1949). About thirty years later, this conjecture was proven to be key for the understanding of Quasicrystals (QC) formation (Shechtman et al. in Phys Rev Lett 53:20, 1951–3, 1984). More recently, it has been found that a few tens to thousand ppm of solute elements in Al-base and Au-base alloys can influence the nucleation and growth of the primary fcc phase via mechanisms involving ISRO and QC formation. ISRO has also been found to limit the mobility, and thus diffusion, of atoms in the liquid. This can lead to out-of-equilibrium conditions, e.g., the formation of metastable phases or supersaturated solid solution, at reduced velocity compared to alloys where ISRO is not predominantly present. Finally, there are several experimental evidences that ISRO is also responsible for twinned dendrites formation in Al alloys. The present contribution summarizes these recent findings and points out the implications that these might have in the field of solidification and additive manufacturing.

I. INTRODUCTION

SOLIDIFICATION of metallic alloys is usually assumed to occur from a fully disordered liquid. The solid–liquid interface at the atomic scale is considered to be diffuse over a thickness, $\delta_{s\ell}$, on the order of nanometer, with many sites where atoms in the liquid can attach to the solid.[1,2] Provided that the velocity $v*$ of the solid-liquid interface is one or two orders of magnitude smaller than $D_\ell/\delta_{s\ell}$, where D_ℓ is the solute diffusion coefficient in the liquid, the solid–liquid interface is close to equilibrium and solidification microstructures are governed by diffusion of solute elements in the liquid and capillarity effects.

Dendrites of the primary phase grow along minima of what is called the solid–liquid interface stiffness, an entity which is deduced from the orientation-dependent solid–liquid interfacial energy, $\gamma_{s\ell}(\boldsymbol{n})$, where $\boldsymbol{n}$ is the unit direction vector.[3] Minima of the interface stiffness usually correspond to maxima of the interface energy, but not always. Under isothermal conditions, equiaxed dendrites develop tips from the most highly curved regions of a nearly spherical solid nucleus. In cubic metals, these growth directions usually correspond to $\langle 100 \rangle$ crystallographic directions of the solid.

When the solid–liquid interfacial energy of the solvent has a weak anisotropy, e.g., aluminum with about 1 pct anisotropy of $\gamma_{s\ell}$,[4] non-cubic or non-metallic solute elements can modify the anisotropy and the shape of the solid nucleus. This can induce a Dendrite Orientation Transition (DOT) from $\langle 100 \rangle$ to $\langle 110 \rangle$, first observed in Al-Zn alloys when the Zn composition increases from 25 to 60 wt pct.[5] A similar transition has been evidenced recently in Al-Ge when the Ge composition increases from 20 to 46 wt pct.[6] In both cases, the DOT has been interpreted as a change of the anisotropy of $\gamma_{s\ell}$ induced by solute elements, when their composition is high enough.

On the other hand, are all these considerations still valid when atoms in the liquid are not fully disordered? Frank [7] already postulated in 1952 that Icosahedral Short Range Order (ISRO) of atoms in the liquid could

M. RAPPAZ is with the Ecole Polytechnique Fédérale de Lausanne, Institute of Materials, Station 12, 1015 Lausanne, Switzerland. Contact e-mail: michel.rappaz@epfl.ch. PH. JARRY is with Constellium C-TEC, Centr'alp, 725 rue Aristide Bergès, CS10027, Voreppe, 38341, France. G. KURTULDU is with the Laboratory of Metal Physics and Technology, Department of Materials, ETH Zurich, 8093 Zurich, Switzerland. J. ZOLLINGER is with the Department of Metallurgy & Materials Science and Engineering, Universitè de Lorraine, Institut Jean Lamour, Allèe André Guinier - ARTEM Campus, 54000, Nancy, France.

explain the large undercoolings measured by Turnbull and Fisher.[8] ISRO was confirmed later by several observations. First of all, ISRO is key to explain the formation of Quasicrystals (QC), first discovered in 1984 by Shechtman *et al.* [9] in Al-Mn, and then found in many other systems. On the other hand, several intermetallic phases, such as Al_7Cr,[10] $Al_4(Cr,Fe)$,[11] Au_4Al,[12] Mg_2Zn_{11}[13] and many others,[14] also exhibit icosahedral motifs in their unit cell. Icosahedral ordering in the liquid phase was also measured by small angle neutron scattering in deeply undercooled liquid forming $Al_{13}Fe_4$ and $Al_{74}Co_{26}$ QC's.[15] The effect of Cr on local ordering in Al-Zn liquid was also modeled by *ab initio* calculations [16, 17]: chromium induces ISRO as well as Icosahedral-based Medium-Range Order (IMRO) of atoms in the liquid. The similarities between ISRO motifs in undercooled liquids and the structure of QC's explain the low solid–liquid interfacial energy of QC's as compared with that of their crystalline approximants.[18,19] This makes QCs the most likely candidates to nucleate initially in an undercooled metallic liquid.

ISRO typically occurs when local covalent bonding is induced around some solute elements, or viewed from an electronic point of view, when a pseudo-gap forms near the Fermi energy level.[20] Although ISRO of atoms cannot be strictly compared to strongly bonded molecules, clustering of atoms around ISRO-inducing elements can have a strong influence on solidification. It can reduce the atomic mobility and thus decrease the diffusion coefficient of atoms in the liquid. It can also influence the attachment kinetics at the solid–liquid interface, as ISRO motifs, in a way similar to ionic-character molecules, have more difficulties to attach to the growing solid compared to individual atoms.

The crystallographic relationships between QCs and the corresponding approximant phases have been studied quite extensively, e.g., for Al-Mn-Si,[18] Al-Ni-Co,[21] or Al-Li-Cu.[22] For example, Goldman and Kelton show the coherent relationship that exists between the bcc phase and the corresponding icosahedral QC (iQC)

in Al-Mn-Si.[23] In Ref. [22], a beautiful SEM picture shows three iQCs formed epitaxially on a single cubic approximant crystal and sharing the same orientation. On the other hand, crystallographic orientation relationships between a matrix phase and icosahedral QC precipitates and/or approximant phase particles have also been investigated, e.g, in Al-Mg-Cu-Ge [24] or Al-Mn-Be-Cu.[25] But to our knowledge, the formation of a primary phase on iQC during solidification and the effect of ISRO on the growth of the primary phase have not been investigated before the first publication by Kurtuldu *et al.* on Al-Zn with minor Cr additions.[26] This work has opened a new field of interest in solidification, but has also raised many questions regarding the effect of trace elements on the nucleation and growth morphology in metallic alloys.

The present contribution has the goal to summarize some of the recent findings regarding the effect of ISRO-inducing trace elements on the solidification of metallic alloys. As this field is fairly new, there are many open questions that remain to be addressed. These will be mentioned in the conclusion of the paper, while the previous sections are structured as follows. In Section II, the geometrical relationships between the fcc unit cell and the icosahedron are recalled. These will be helpful to present the effect of ISRO on nucleation and growth, respectively in Sections III and IV. It will be shown in Section V that ISRO slows down diffusion in the liquid, opening new possibilities to induce solute trapping at reduced speed, e.g., in additive manufacturing. Finally, Section VI will present some experimental evidences that link the formation of twinned dendrites in Al alloys with ISRO.

II. RELATIONSHIPS BETWEEN ICOSAHEDRON AND FCC STRUCTURE

A regular icosahedron exhibits 20 equilateral triangular facets, 12 vertices and 30 edges (Figure 1(a)). The
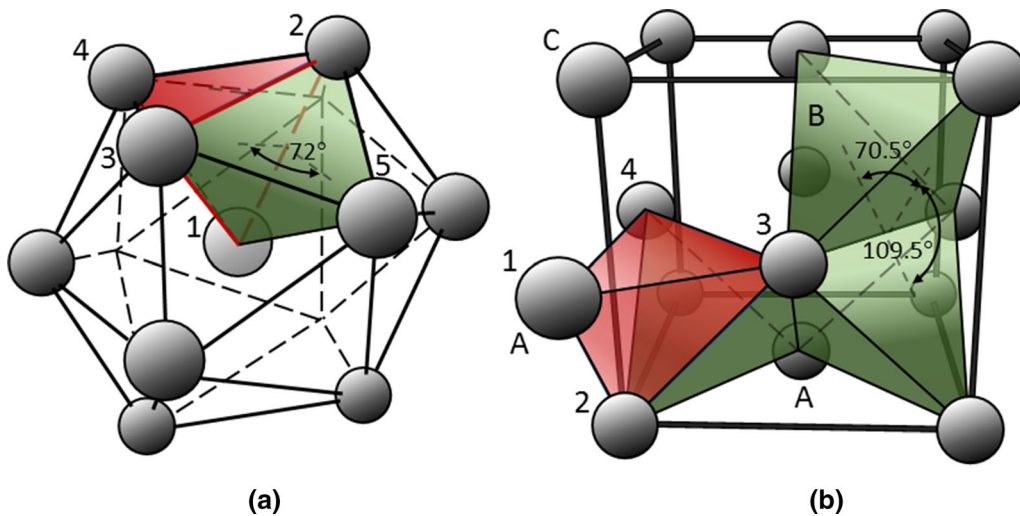

(a)　　　　　　　(b)

Fig. 1—(*a*) Icosahedron with two nearest-neighbors of its 20 tetrahedra shown in red and green; (*b*) unit cell of the fcc structure with representation of three of the 8 tetrahedra made of {111} planes and ⟨110⟩ edges (in green) and one stacking fault induced by the attachment of one tetrahedron (in red).

axes linking opposite vertices correspond to fivefold symmetry axes, those going through the centers of opposite facets/edges correspond to threefold/twofold symmetry axes, respectively. If atoms of size 1 are located at the twelve vertex positions, a close pack structure can only be reached if an atom of size 0.902 is at the center (atom labeled "1" in Figure 1(a)), *i.e.,* about 10 pct smaller. The tetrahedra formed by the center and three neighbor vertices, *e.g.,* atoms 1-2-3-4 or 1-2-3-5, are therefore, slightly distorted compared to the {111} tetrahedra of the fcc structure. Considering the three "internal" planes of a tetrahedron (*e.g.,* 1-2-3, 1-2-4 and 1-3-4), their mutual angles are 72 deg, instead of 70.5 deg for a regular tetrahedron, since five of them around a fivefold symmetry axis make 360 deg. The angle between one of these "internal" planes and the external triangular facet of the icosahedron (2-3-4) is only 69.1 deg. Please note that the 20 slightly distorted tetrahedra of the icosahedron are linked by faces to their nearest-neighbors (nn), as shown by the red and green tetrahedra in Figure 1(a).

The fcc unit cell shown in Figure 1(b) can be viewed as a succession of densely packed atoms arranged in {111} planes with a sequence ABCABC…* The unit cell

---

*In Figure 1(b), the labeling of ABC is made according to the set of {111} planes parallel to the plane given by atoms 2-3-4, *i.e.,* atom A belongs to the first layer, 2-3-4 is layer B and the atom at the top, front left corner to layer C.

---

contains 8 tetrahedral sites delimited by {111} planes with ⟨110⟩ edges. Three of them are represented in green in Figure 1. The angles between {111} planes are either 70.5 deg or 109.5 deg. Please note that, unlike the icosahedron, these tetrahedra only touch along edges, and not faces, in the fcc structure. Should another regular tetrahedron attach to this structure with a coinciding {111} plane (red tetrahedron in Figure 1), this would create a stacking fault possibly leading to the formation of a twin with a {111} planes sequence ABCA**B**ACB… Unlike many other fcc metals, twinning in aluminum is not favored since it is characterized by a high energy: 0.119 J/m^2 for a coherent twin, compared to 0.015 or 0.01 J/m^2 for Au or Ag, respectively (see the compilation in Table IV of [27]).

Except for the small distortion of the tetrahedra of the icosahedron, two neighbors (red and green in Figure 1(a)) are in a twin relationship if one considers that their faces are like 3 nn atoms of {111} planes in a fcc structure. As a matter of fact, it was found in the 1960's that nanocrystals of pure Au or Ag are Multi-Twinned icosahedra or decahedra Particles (MTP), rather than Wulff-type morphologies.[27] This is due to the lowest solid-vapor interfacial energy of {111} planes: fcc nanocrystals tend to exhibit {111} external facets in order to minimize their interfacial energy, the misfit angle between 72 and 70.5 deg. being compensated by strain energy. Since elastic energy goes with the third power of the radius, while the surface energy gain is proportional to the second power of the radius, Ino [27] calculated the critical transition radius between MTP

icosahedral and Wulff equilibrium shapes (about 5.35, 3.8 and 1.45 nm for Au, Ag and Al, respectively). Although they exhibit a similar symmetry, icosahedral MTP's should not be confused with iQC's. On the other hand, the probability of forming MTP's from the liquid phase is nil, since the interfacial energy between the solid and liquid is about one order of magnitude lower than that between the solid and vapor, *i.e.,* the critical transition radius between MTP and Wulff morphologies becomes on the order of the atomic spacing.

III. EFFECT ON NUCLEATION

The discovery in 2013 that ISRO can influence the nucleation of fcc alloys was a serendipity event while studying the effect that some trace elements can have on the growth morphology of Al dendrites.[26,28] Choosing Al-20 wt pct Zn alloy because its composition is at the limit of the DOT between ⟨100⟩ and ⟨110⟩ dendrites,[5] it was found that columnar structures produced by directional solidification were significantly influenced by the addition of 0.02 to 0.1 wt pct Cr (see Section IV). To eliminate the effect of the thermal gradient, equiaxed experiments under nearly uniform temperature were then performed, without and with Cr addition.[26] As shown in Figure 2, it was found that 0.1 wt pct Cr: (i) drastically reduces the grain size; (ii) induces an abnormal percentage of twinned grain boundaries; (iii) induces multiple-twinning relationships among nearest-neighbor (nn) grains compatible with the geometry of the icosahedron or interlocked double-icosahedron (two icosahedra connected with a common pentagon). The heteroepitaxy relationship between the icosahedron and fcc is:

Al – 20% Zn (G ≈ 0)
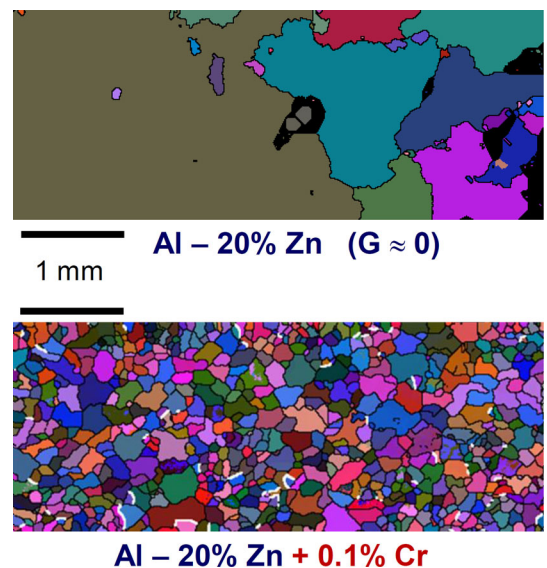
1 mm

Al – 20% Zn + 0.1% Cr

Fig. 2—EBSD false-color grain structure maps of Al-20 wt pct Zn without (top) and with (bottom) the addition of 0.1 wt pct Cr. Twinned grain boundaries detected with an accuracy of 5 deg are shown in white. Adapted from Ref. [28].

$$\langle 111 \rangle_{\text{fcc}} // \langle 3 \text{ - fold axes} \rangle_{\text{ico}} \text{ and } \langle 110 \rangle_{\text{fcc}} \perp \langle 2 \text{ - fold axes} \rangle_{\text{ico}} \quad [1]$$

Besides geometrical considerations of nn-MT grains, Kurtuldu et al. [26] also supported their interpretation with three more arguments: (i) thermodynamic calculations show that the liquidus of $Al_{13}Cr_2$ is first crossed during the solidification of Al-20 wt pct Zn-0.1 wt pct Cr; (ii) $Al_{100-x}Cr_x$ with $7 \leq x \leq 20$ are among the first discovered icosahedral quasicrystals [18]; and (iii) the

approximant $Al_{13}Cr_2$ ($x = 13.3$) has many icosahedral building blocks in its unit cell. [10]

The so-called "iQC-mediated nucleation" of the fcc phase in Al-Zn-Cr is summarized in Figure 3 with the following steps [29]: ISRO motifs around Cr atoms (a) aggregate into IMRO clusters and form iQC's into the liquid (b); as the melt becomes depleted with the peritectic-type Cr element, [30] the fcc phase forms on the facets of iQC's with the heteroepitaxy relationships (1)** (c); upon

---

**In Figure 1, one of the 20 external facets of the iQC (or ISRO) corresponds to atoms 2-3-4 of the red tetrahedron and the fcc crystal forming on this facet would have the crystallographic structure shown in (b).

---

further cooling, the iQC's can even disappear by peritectic transformation (d), leaving only the "trace" of the iQC template via MT relationships of fcc grains.

One year later, a similar mechanism was evidenced in yellow gold (Au-12.5 wt pct Cu-12.5 wt pct Ag) when very small amounts of Ir are added to the melt. [29] Iridium is a known impurity found in some gold ores, in particular in California, and can be detrimental to their plastic behavior (e.g., coinage) when present in large amounts. [31] Although there is no reported iQC for such alloys, adding a few tens of ppm of iridium in gold alloys is a well-known practice in jewelry and dental applications to refine the grain size. [32] Figure 4 shows the effect of increasing additions of Ir to yellow gold melts, solidified otherwise under identical conditions. [29] In these false-color EBSD grain structures, twinned grain boundaries are indicated in white. Besides the drastic grain refinement with increasing amounts of Ir, the percentage of twinned grain boundaries is increased from less than 1 pct without added Ir to 11 pct with 200 ppm of Ir.

The grain size in the 200 ppm Ir specimen is so small that many clusters of nn-MT grains can be easily detected. In Figure 5, 9 nn grains exhibit multiple twin relationships which can be explained with the fivefold
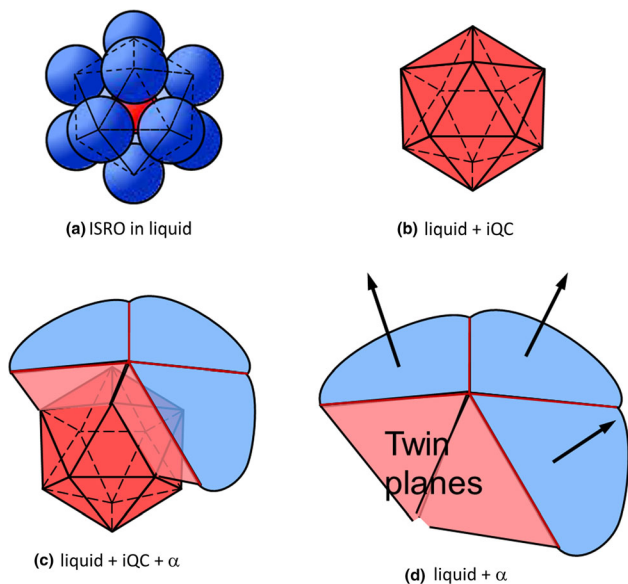

Fig. 3—Schematic representation of the ISRO- or iQC-mediated nucleation mechanism: (a) formation of ISRO in the liquid; (b) formation of iQC on which (c) the fcc phase can form with heteroepitaxy relationships with the icosahedron, producing MT grains; (d) further growth of the fcc phase and disappearance of the iQC template by peritectic transformation. [29]
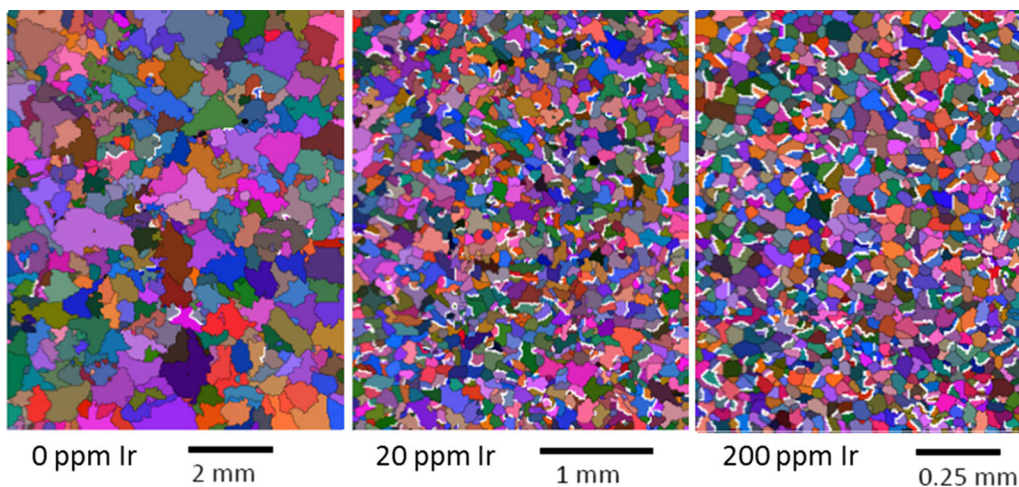

Fig. 4—EBSD false-color grain structure maps of Au-12.5 wt pct Cu-12.5 wt pct Ag with various additions of Ir. Twinned grain boundaries detected with an accuracy of 5 deg. are shown in white. Adapted from Ref. [29].
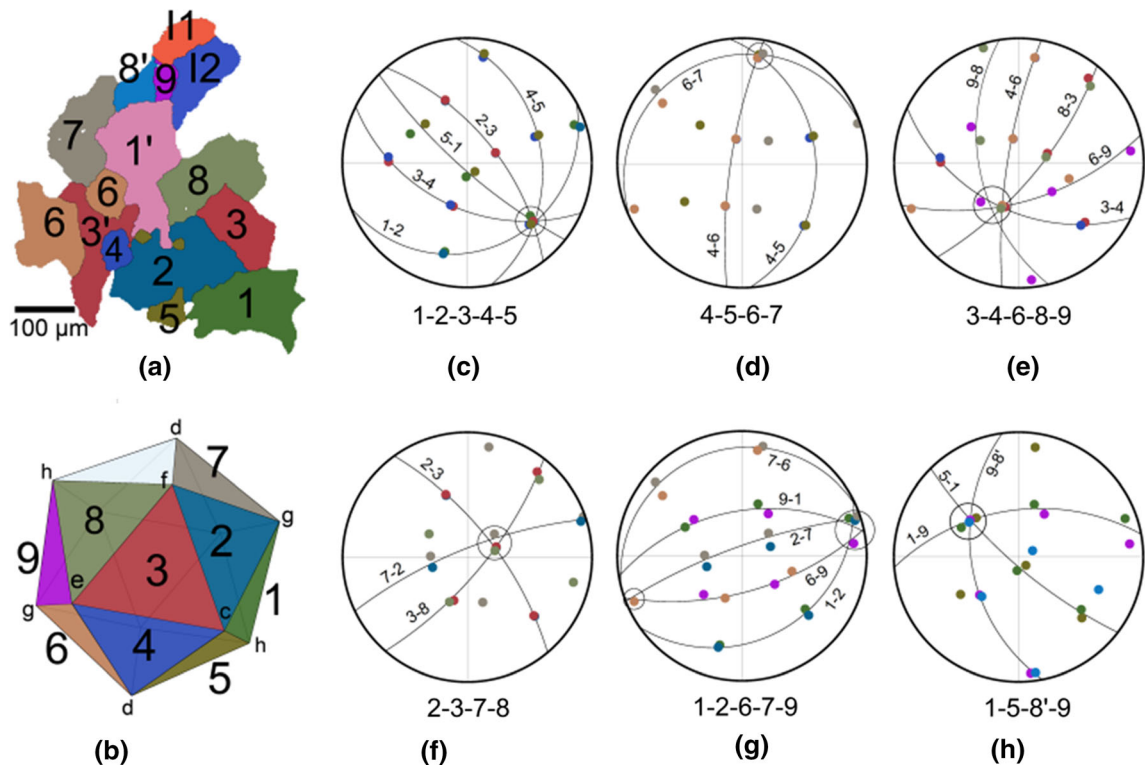
Fig. 5—(*a*) EBSD false-color grain structure maps of 9 grains in Au-12.5 wt pct Cu-12.5 wt pct Ag with 20 ppm Ir. The ⟨110⟩ pole figures of sets of MT grains are shown in (*c* through *h*), with the common ⟨110⟩ direction circled in each figure and indication of the {111} twin or near-twin planes by arcs of circle. In (*b*), an icosahedron has been schematically drawn in a position such that the six 5-fold symmetry axes labeled (c through h) approximately correspond to the common ⟨110⟩ axes of the fcc grains, and with corresponding facets of the same color as grains in (a). Adapted from Ref. [29].

symmetry of the icosahedron. For example, grains 1 to 5 in (a) share a common ⟨110⟩ direction in the ⟨110⟩ pole figure (circled in (c)) and 5 twin or near-twin[†] {111}

[†]A near-twin relationship has been defined in [26] as a twin relationship + a rotation of about 7 to 8 deg around a common ⟨110⟩ direction. This rotation corresponds to the cumulated angle difference between 5 tetrahedra of the icosahedron (360 deg) and 5 regular {111} tetrahedra of the fcc structure (352.5 deg).

---

planes (arcs of a circle) separated by about 72 deg. between grains 1-2, 2-3, 3-4, 4-5 and 5-1. Please note that only the common ⟨110⟩ directions in these {111} twin planes have been kept in the pole figure in order to make it simpler to visualize. The other ⟨110⟩ pole figures illustrate the other twinning relationships between four or five grains sharing a common ⟨110⟩ direction. These common ⟨110⟩ directions correspond to the six 5-fold symmetry axes of an icosahedron, shown in (b) with a viewing angle where these axes labeled (c) to (h) correspond roughly to the pole figures of the fcc grains.

Figure 6 is a proof of the relationship between the orientation of the 9 MT grains of Figure 5 and an icosahedron template, as described in Figure 3. In this ⟨110⟩ pole figure of the fcc grains, the open squares correspond to the common ⟨110⟩ directions circled in Figures 5(c) through (h). The filled triangles have been
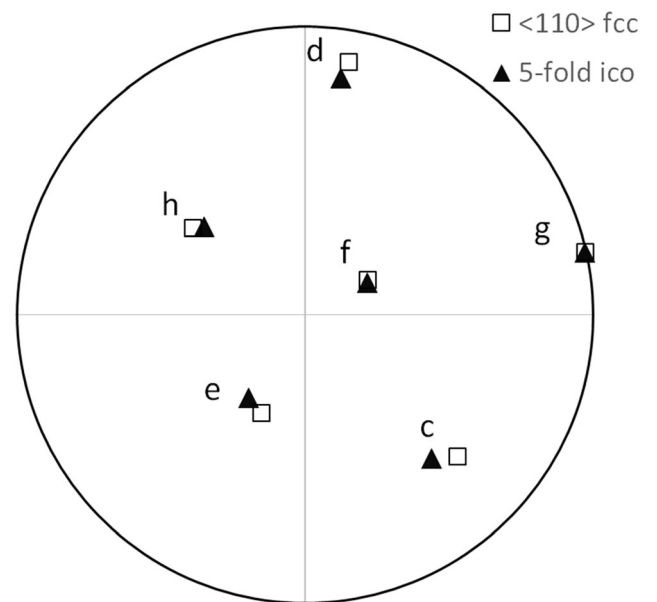

Fig. 6—Stereographic projection corresponding to the pole figures of Figure 5, where the common ⟨110⟩ directions seen in c–h are shown as open squares. The filled triangles have been calculated from the directions of the fivefold symmetry axes of an icosahedron, with an exact correspondence between ⟨110⟩_fcc and ⟨fivefold axis⟩_ico for (g) and the best agreement for the other ⟨fivefold axes⟩_ico directions.

calculated from the angles between the fivefold symmetry axes of the icosahedron (63.43 or 116.57 deg). The position of the fivefold axis (triangle g) has been superimposed to the common ⟨110⟩ direction in Figure 5(g), and the other fivefold axes of the icosahedron have been calculated so as to have the best correspondence with the other common ⟨110⟩ directions of the fcc grains. There is no doubt that these fcc grains have nucleated from an icosahedron template, with the heteroepitaxy relationships (1), especially if one accounts for the cumulation of misfit angles between the tetrahedra of the fcc structure (70.5 deg) and those of the icosahedron (72 deg). Whether these fcc grains form with the same sequence shown in Figure 3 as suggested for Al-Zn-Cr, *i.e.*, iQC-mediated nucleation, or directly from an "ISRO-mediated nucleation" mechanism since no iQC has been reported for Au-Cu-Ag-Ir, remains an open question.

To search for other potential ISRO-inducers in gold alloys, a literature search of Au-base QC's was made. The Tsai-type QC [33] $Au_{51}Al_{34}Yb_{15}$ and approximant $Au_{51}Al_{35}Yb_{14}$ have been studied by Deguchi *et al.* [34] and Matsukawa *et al.*[35] Since the Al composition is about twice (in atomic percent) that of Yb, a few percents of an alloy made of Al and Yb with a 2:1 atomic ratio was added to yellow gold.[36] Adding the same amount of only Yb or Al did not produce any significant effect on the final grain size. Adding 2 wt pct of Al_2Yb refined the grain structure and induced an abnormal percentage of twin boundaries (Figure 7). However, the grain size was not uniform and very often a fairly large grain was surrounded by smaller ones with a twin relationship, *e.g.*, grain 1 surrounded by twinned grains 2, 3 and 4 in Figure 7. These small ones often repeated at several locations (*e.g.*, grain 3 at the edge and center of grain 1, or grain 4 at two locations at the periphery of grain 1 in Figure 7). Again, the icosahedral

and heteroepitaxy relationships (1) for these four grains are clearly shown by the corresponding ⟨110⟩ pole figure in Figure 7: the three {111} twin planes between grains 1 and 2, 1 and 3 and 1 and 4 are shown with dashed lines and the same color code as in the false color EBSD figure. The common (or near-common) ⟨110⟩ directions in these planes are circled and at the crossing of the three {111} twin planes, there are three common ⟨110⟩ directions which must correspond again to fivefold symmetry axes of the icosahedron. These are indicated with small pentagons in Figure 7 and correspond well to these three common ⟨110⟩ directions.

IV. EFFECT ON GROWTH

In the previous section, we have seen how ISRO in the liquid can refine the grain size via an iQC- or ISRO-mediated nucleation mechanism, producing multiple twin relationships among nn fcc grains which can only be explained with the help of the heteroepitaxy relationships (1) between fcc and icosahedron.

But ISRO can also have an influence during the growth of the fcc phase. Looking more closely at Figure 7, the mechanism of grain refining and twinning looks slightly different from that already observed in Al-Zn-Cr or Au-Cu-Ag-Ir alloys. The non-uniform grain size and the alternated sequence of twinned grains around a larger one seem to indicate that twinning induced by Al_2Yb occurred *after* some fcc grains have grown up to a certain size. As Au-Yb and Au-Al are both eutectic-type phase diagrams, ytterbium and aluminum are rejected during the growth of these large grains. Once the composition is high enough, twinning occurs probably with a stacking fault mechanism similar to that shown in Figure 1, *i.e.*, one of the tetrahedra of the ico, e.g., 1-2-3-4 in red, attaching to a {111} tetrahedron of the fcc phase with its external facet
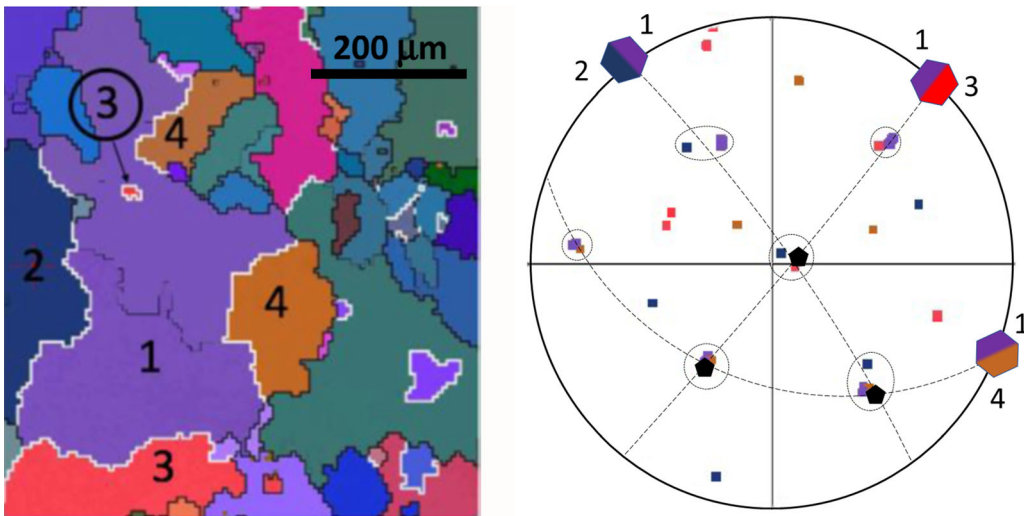

Fig. 7—EBSD false color grain structure of Au-12.5 wt pct Cu-12.5 wt pct Ag with 2 pct Al_2Yb addition to the melt. Twin grain boundaries are indicated in white. The ⟨110⟩ pole figure of grains 1 to 4 are shown on the right with the common {111} plane between 1 and 2, 1 and 3 and 1 and 4 indicated by dashed arcs of circle. The common ⟨110⟩ directions are circled. At the crossing of common {111} twin planes, there are 3 common ⟨110⟩ directions for grains 1-2-3, 1-2-4 and 1-3-4 and the small pentagons correspond to the calculated position of three of the 5-fold axes of an icosahedron. Adapted from Ref. [36].

2-3-4. It should be kept in mind that, unlike Bergman- or Mackay-type iQC's, a Tsai iQC contains a tetrahedron inside the first icosahedral layer.[33] Although the detailed mechanism remains to be clarified to explain the effect of Al₂Yb on Au-base alloys, twinning seems to occur during growth, rather than at the nucleation stage. This mechanism will be called "ISRO-induced stacking fault". It should also be mentioned that a similar alternation of MT grains has been observed in pink gold (Au-20.5 wt pct - Cu-4.5 wt pct Ag) with 100 ppm of Ir, but rapidly solidified.[37]

The effect of ISRO on the growth of fcc dendrites can be best described for columnar structures, when nucleation of new grains is avoided. Kurtuldu *et al.* have observed the effect of 0.02-0.1 wt pct Cr addition on columnar dendrites during Bridgman solidification of Al-20 wt pct Zn.[38] Once steady-state conditions were reached, a quench was made and the quenched mushy zone was observed ex situ using X-ray microtomography. The 3D stack of images can then be cut along any desired plane and correlated with SEM-EBSD orientation measurements. As this alloy has a composition below the DOT,[5] it was confirmed that, without Cr, dendrites solidify with a trunk oriented along $\langle 100 \rangle$, as shown in Figures 8(a) through (c). In (a), a longitudinal cut has been made parallel to the trunk direction, *i.e.,* along the dashed white line shown in the transverse section (b). The trunk is slightly oriented toward the left, as compared with the
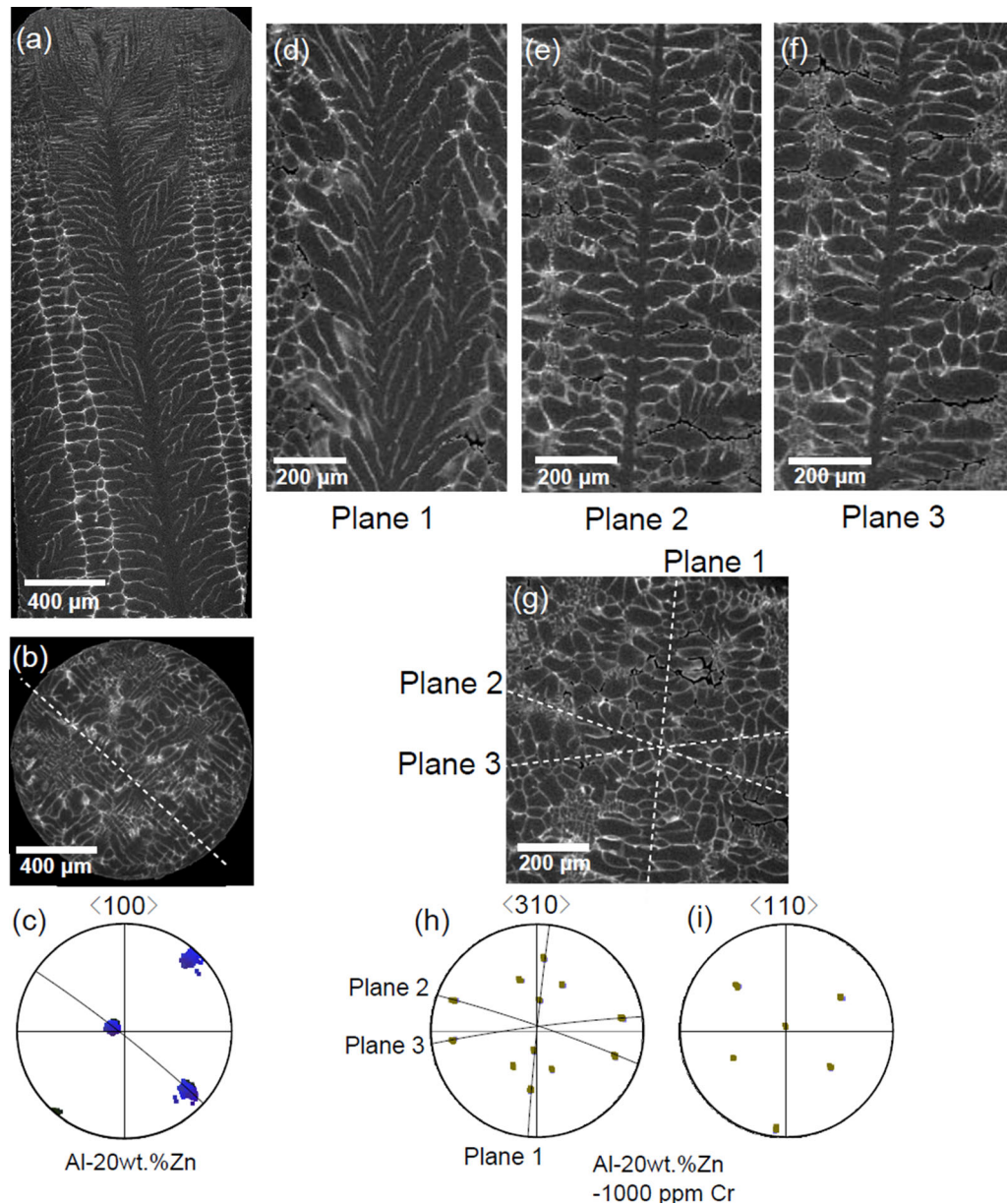

Fig. 8—2-Dimensional views of X-ray microtomography analyses of Al-20 wt pct Zn alloys solidified in a Bridgman furnace at 67 μm/s in a 100 K/cm thermal gradient, (a) through (c) without Cr, (d) through (i) with 0.1 wt pct Cr. (a) and (d) through (f) correspond to longitudinal sections, (b) and (g) to transverse sections and (c), (h) and (i) are relevant pole figures corresponding to the transverse sections (i.e., thermal gradient located at the center).[28]

thermal gradient which is vertical. Secondary arms in (a) have a seaweed appearance but are more or less perpendicular to the trunk. As shown in the $\langle 100 \rangle$ pole figure (c), for which the axes correspond to the transverse section (b), the trunk is definitely oriented along a $\langle 100 \rangle$ direction, as expected for this Zn composition. In the same way, secondary arms point also along $\langle 100 \rangle$ directions.

Under identical Bridgman conditions, the addition of 0.1 wt pct Cr changes the morphology of the columnar dendrites (Figures 8(d) through (i)). After identification of the dendrite trunk position in the cross-section (g), 3 longitudinal sections parallel to the trunk have been done along traces indicated with the white dashed lines in (g). These sections are shown in (d to f), while $\langle 310 \rangle$ and $\langle 110 \rangle$ poles figures corresponding to the transverse section (g) are shown in (h) and (i), respectively. First, it appears in (i) that the trunk is no longer $\langle 100 \rangle$ as in (c), but is now $\langle 110 \rangle$. With such a low level of Cr, it cannot be argued that this change of orientation from $\langle 100 \rangle$ to $\langle 110 \rangle$ is due to a change of the anisotropy of $\gamma_{s\ell}$, as observed when the Zn composition is increased from 20 to 60 wt pct.[5] Furthermore, chromium is a cubic-type element. And finally, as reported in,[38] a $\langle 100 \rangle$ trunk orientation is retrieved at higher speed (about 1 mm/s) even with 0.1 wt pct Cr (see Figure 12). Therefore, the orientation change observed in Figure 8 when Cr is added can only be explained by a *kinetic effect* induced by Cr and associated with an increase of ISRO in the liquid.

Secondary arms are also affected by the addition of Cr and ISRO, as can be seen in Figure 8. Along longitudinal planes 2 and 3 (Figures 8(e) and (f)), secondary arms are nearly perpendicular to the trunk. However, in plane 1 (Figure 8(d)), they have a palm-tree appearance. The corresponding plane traces have been drawn in the $\langle 310 \rangle$ pole figure (h): along each plane 2 or 3, two sets of $\langle 310 \rangle$ directions are visible at 77 deg. from the $\langle 110 \rangle$ trunk direction. In plane 1, however, two sets of two $\langle 310 \rangle$ directions at 26.4 and 63.4 deg from $\langle 110 \rangle$ are intersected‡.

---

‡Each $\langle 100 \rangle$ direction, making an angle of either 45 or 90 deg. with respect to the $\langle 110 \rangle$ trunk direction, is surrounded by a quadruplet of $\langle 310 \rangle$ directions at 18.4 deg., clearly seen in Figure 8.

Although $\langle 310 \rangle$ directions cannot be clearly identified in the palm-like morphology of Figure 8(d), the arms in this section are very inclined compared to those in plane 2 or 3 (typically 23 to 37 deg from the trunk) and are definitely closer to $\langle 310 \rangle$ than $\langle 110 \rangle$.

Kurtuldu *et al.* [38] have interpreted these orientation changes of the trunks and arms as a function of the Cr composition and velocity as follows. Cr is a peritectic-type element.[30] As the velocity is increased, the composition of Cr ahead of the tip decreases. This can explain why a $\langle 100 \rangle$ trunk direction is retrieved at a higher velocity, even with 0.1 wt pct Cr, as the percentage of ISRO motifs ahead of the interface is decreasing. Similarly, at lower velocity, the Cr composition in between the trunks is also lower compared to the $\langle 110 \rangle$ dendrite tip, thus explaining why

secondary arms are already closer to $\langle 100 \rangle$, *e.g.,* $\langle 310 \rangle$, than $\langle 110 \rangle$. The detailed mechanism of how ISRO motifs in the liquid modify the attachment kinetics remains to be determined, a tentative conjecture being given in [38].

A similar growth direction change induced by ISRO has been observed in rapidly solidified Au-20.5 wt pct - Cu-4.5 wt pct Ag with 0.01 wt pct Ir.[37] Droplets of a few mm in diameter were allowed to fall on a Cu chill surface, thus giving cooling rates on the order of -10^4 K/s close to the chill and -10^2 K/s at the top surface of the fallen drop. Figure 9 shows BSE-SEM images taken close to the chill where columnar grains are observed, and near the top surface where equiaxed grains have formed. The top/bottom rows show these microstructures in the Ir-free specimen and in one with 0.01 wt pct Ir, respectively. The small insert in each micrograph is an enlargement of the internal grain structure.

The Ir-free specimen shows a "normal" dendritic grain structure with a Columnar-to-Equiaxed Transition (CET). In the columnar zone, grain competition favors those having a $\langle 100 \rangle$ orientation most closely aligned with the thermal gradient (horizontal in Figure 9). The inverse pole figure corresponding to this columnar zone (Figure 10(a)) clearly confirms the formation of a $\langle 100 \rangle$ texture along the thermal gradient direction. The equiaxed grains are fairly coarse and have also an internal dendritic structure, with segregation of Cu and Ag in between dendrite arms.

With 0.01 wt pct Ir, the situation is markedly different. As observed under lower solidification rate (Section III), such alloys exhibit a much finer equiaxed grain structure with many MT relationships compatible with the iQC- or ISRO-mediated nucleation mechanism. Their internal structure is more globular than dendritic. But two new phenomena have been observed under rapid solidification conditions. Firstly, the microstructure exhibits a dual fcc-phase structure in both the columnar and equiaxed zones. It is made of very fine Cu-rich dendrites or particles and of Au-rich grains. These Cu-rich dendrites are most often twinned, have no orientation relationship with the Au-rich grains and are much coarser than precipitates forming from solid state precipitation. Therefore, they clearly solidify from the liquid state like the Au-rich grains, most probably before. This dual fcc phase structure could be explained by an increase of ISRO motifs in the liquid around Ir atoms slowing down diffusion (see next Section) and resulting in dynamic heterogeneities in the liquid. These heterogeneities would be at the origin of a spinodal decomposition, as already suggested in[39] to explain iQC-mediated nucleation, thus producing Cu- and Au-rich regions. The second effect induced by 0.01 wt pct Ir addition concerns the internal structure of the columnar grains. As can be seen in the small inserts of Figure 9, $\langle 100 \rangle$ dendrites are replaced by a cellular-type morphology when Ir is added, growing along the thermal gradient. This morphology exhibits a $\langle 111 \rangle$ texture as observed in the inverse pole figure of Figure 10(b).
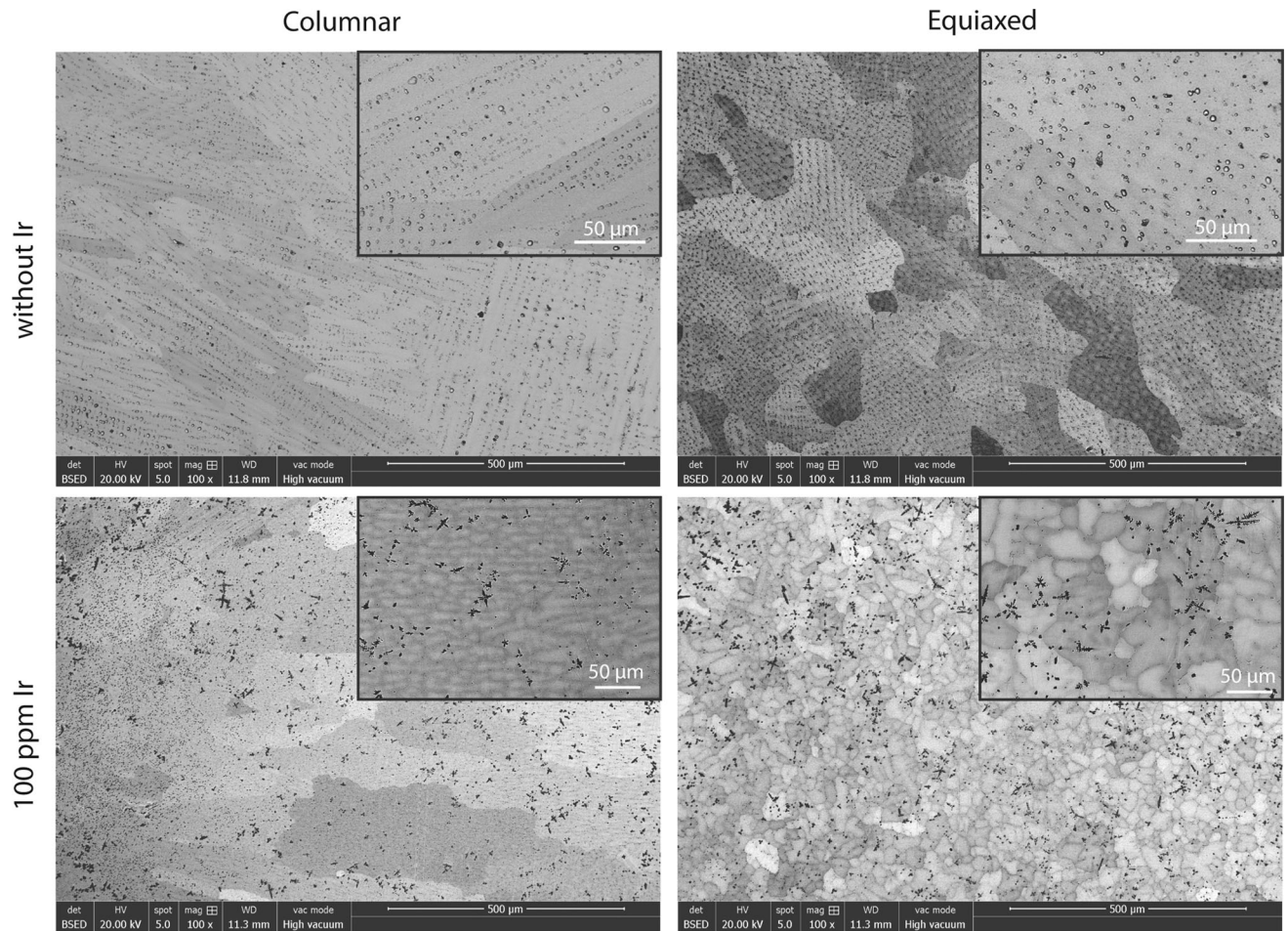
Fig. 9—SEM-BSE images Au-20.5 wt pct Cu-4.5 wt pct Ag without (top) and with (bottom) 100 ppm of Ir added to the melt. The small droplet of each alloy has been solidified rapidly on a Cu substrate, producing a columnar structure close to the chill (left) and equiaxed grains near the top (right). The small inserts show magnification of the microstructure. Black dots correspond to Cu-rich dendrites/particles, while Au-rich grains appear with various gray levels. The thermal gradient is horizontal.[37]
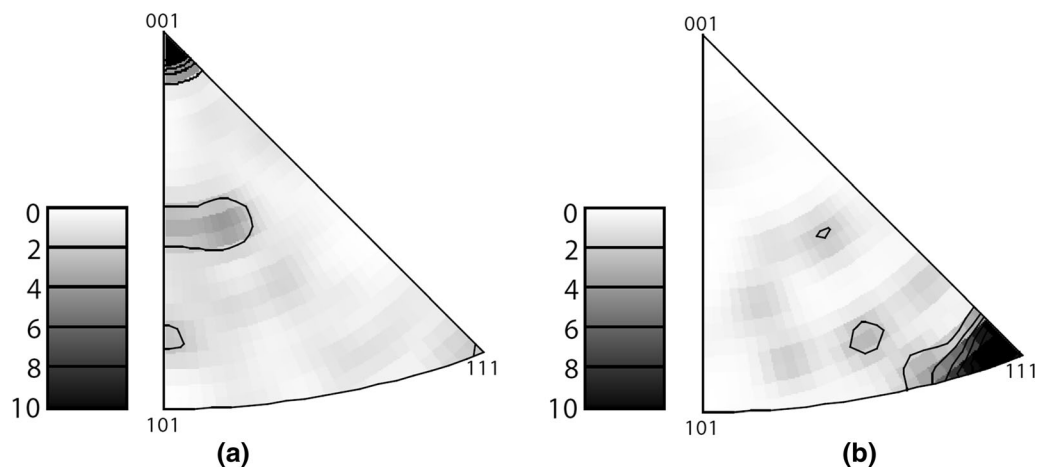

Fig. 10—Inverse texture pole figures of the columnar zones in Au-20.5 wt pct Cu-4.5 wt pct Ag (Figure 9) without (a) and with (b) 100 ppm Ir.[37] In this unit triangle of the fcc structure, the grey level index corresponds to the probability to have the thermal gradient aligned with an ⟨hkl⟩ direction of the columnar grains.

The detailed mechanism by which 100 ppm Ir modifies the morphology and texture of the primary phase remains to be elucidated, but considering the effect it has on iQC- or ISRO-mediated nucleation, it is most certainly associated with the increased tendency to form ISRO motifs in the liquid. This effect as well as the two-phase spinodal-type decomposition are most probably associated with the attachment kinetics and reduced mobility of icosahedral-type motifs in the liquid.

V. EFFECT ON MOBILITY

When local covalent bonding occurs around 100 to 1000 ppm of trace elements in the liquid, this "cloud" of atoms must be characterized by a reduced mobility. Using ab initio calculations, Pasturel and Jakse[16] calculated self-diffusion coefficient of Al and Cr in $Al_{93}Cr_7$ melt, as well as the melt viscosity as a function of temperature. The liquidus temperature corresponding to this composition is about 750 °C (1023 K). While an Arrhenius behavior was observed above 1000 K, the Stokes-Einstein relationship is no longer respected for Al, while it still is for Cr, in the undercooled melt. Upon cooling, these authors concluded that icosahedral-based medium range order (IMRO) is initiated around Cr atoms. This can be correlated with the occurrence of what they call "dynamic heterogeneities" (DHs) in the melt, where Al atoms are still characterized by fast dynamics, while Cr-rich regions exhibit slow dynamics. As a matter of fact, the calculated self-diffusion coefficient for Al atoms at the melting point of pure Al is close to the value used in many solidification calculations (3×10^{-9} m^2/s), but that of Cr is about 5 times lower. Such dynamic heterogeneities induced by ISRO and IMRO could also explain the spinodal decomposition observed in Au-alloys under rapid solidification conditions (see Figure 9).

Kurtuldu et al. [40] have measured the diffusion coefficient of Zn and Cr in Al-Zn and Al-Zn-0.1 wt pct Cr alloys (see Figure 11). For that purpose, Bridgman solidification of these alloys was performed under stable planar-front conditions. Changing the Zn composition allowed to have steady-state growth at various solidus temperatures. After quenching, the Zn- and Cr-composition profiles in the quenched liquid and in the solid near the interface were measured by Electron Probe MicroAnalyzer (EPMA) and Energy-Dispersive X-ray (EDX) analysis. From these profiles, the thickness D_ℓ/v^* and thus the diffusion coefficients were deduced for each solute species.

As seen in Figure 11, the Cr-free samples (open circles) exhibit a diffusion coefficient $D_{\ell,Zn}$ for zinc that agrees well with previous measurements. With 0.1 wt pct Cr, this diffusion coefficient is reduced by about 25 to 30 pct (filled circles), while that of Cr (filled diamonds) is three times lower. This reduced mobility of Zn and especially of Cr, which has an even lower atomic number than Cr, is attributed to ISRO motifs forming around Cr atoms.
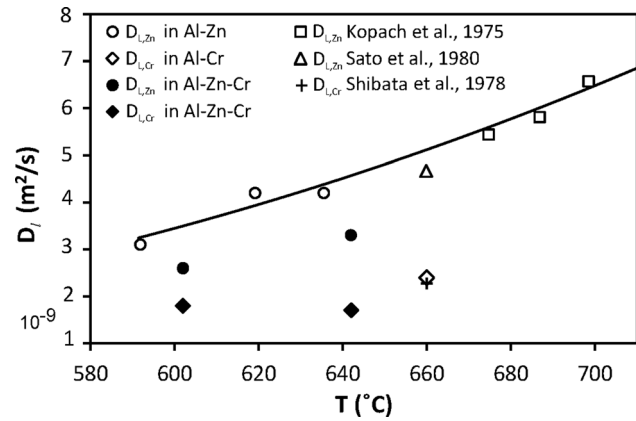

Fig. 11—Diffusion coefficients of Zn and Cr in the liquid for Al-Zn and Al-Zn-0.1 wt pct Cr alloys as measured from the solute profile in the quenched liquid ahead of a planar-front during Bridgman solidification.[40]

VI. POSSIBLE ORIGIN OF TWINNED DENDRITES

As shown in the previous sections, trace elements such as Cr in Al alloys or Ir in Au alloys can induce ISRO-mediated nucleation and/or ISRO-induced stacking fault. Is it possible that this mechanism (and trace elements) could be responsible of twinned dendrites formation in aluminum alloys?

Twinned dendrites, the basic microstructure element of feathery grains, was described by Hérenguel more than 70 years ago.[41] This growth morphology was studied quite extensively over the past two decades, first by Henry et al. [42,43] and then by Salgado-Ordorica et al.[44,45] Based on EBSD, SEM, STEM analyses and phase field calculations, these investigations have shown that a columnar twinned dendrite grows with a ⟨110⟩ trunk, split in its center by a {111} coherent twin and with a mixture of ⟨110⟩ and ⟨100⟩ secondary arms on each side. These secondary arms meet those of neighboring twinned dendrites at incoherent twin planes. The twin boundary energy of the coherent twin plane creates a small cusp at the dendrite tip and during growth, this cusp gets deeper and forms a doublon, as conjectured in Reference [42] and shown later by phase field simulations in Reference [44].

While the growth of twinned dendrites is now better, if not fully, understood, the origin of the twins was still a mystery until the work of Kurtuldu et al.[26] As already mentioned in Section III, ISRO-mediated nucleation was discovered in Al-Zn-Cr after a twinned dendrite was observed in a specimen solidified under nearly nil thermal gradient and minimal convection, two conditions that normally do not favor their formation.

The role of Cr on the formation of twinned dendrites in Al-20 wt pct Zn is demonstrated in Figure 12.[38] Directional solidification (DS) experiments were performed by casting Al-20 wt pct Zn alloy, without and with 0.1 wt pct Cr, in a steel mold. A water jet under the thin bottom steel sheet of the mold induced velocity of the liquidus isotherm of 1 to 2 mm/s in this region. As can be seen in the EBSD reconstructed grain structure of
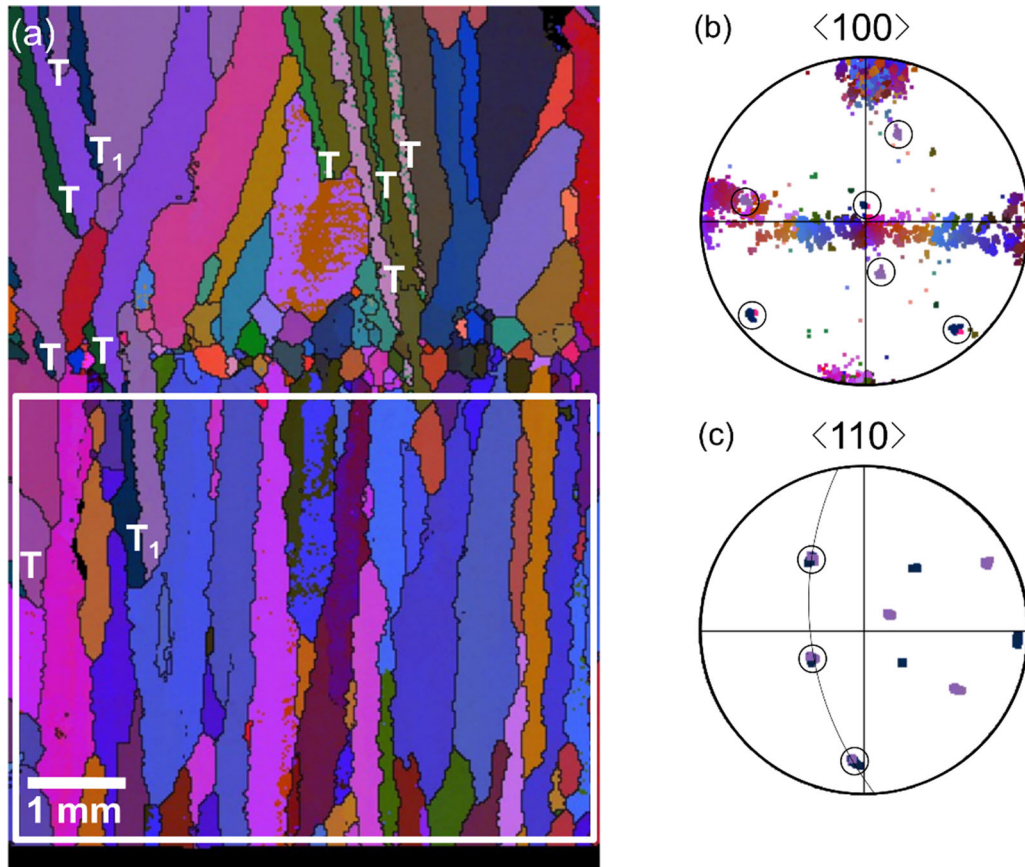
Fig. 12—(*a*) EBSD false color map of a longitudinal section of an Al-20 wt pct Zn-0.1 wt pct Cr specimen directionally solidified. Regular dendritic grains at the bottom exhibit a $\langle 100 \rangle$ texture, as shown in (*b*), while the $\langle 110 \rangle$ pole figure in (*c*) is for the isolated twinned dendrites labelled "T_1". Other twinned dendrites in the upper part of the specimen are clearly visible.[38]

the longitudinal section of this Al-Zn-Cr specimen (Figure 12a), regular grains with a strong $\langle 100 \rangle$ texture first form at the bottom near the steel sheet. The $\langle 100 \rangle$ pole figure of the grains within the white rectangle is shown in (b). This situation is similar to regular dendrites of Al-20 wt pct Zn without Cr addition, and different from the observation of Figure 8, where $\langle 110 \rangle$ trunks are observed with Cr but at lower speed. This has been interpreted as a decrease of the Cr composition ahead of the dendrite tip when the velocity increases,[38] since Cr is a peritectic-type element in Al alloys. However, one twinned dendrite, labeled "T_1", can already be identified in this region. Its $\langle 100 \rangle$ directions are circled in the corresponding $\langle 100 \rangle$ pole figure (b), while the $\langle 110 \rangle$ pole figure shown in (c) for only T_1 clearly shows that this is indeed a twinned dendrite with a nearly vertical {111} twin plane (arc of a circle in (c)). This twinned dendrite extends in the upper part of the specimen, while other twinned grains appear (labeled "T"). Please note that a small layer of nearly equiaxed grains is present just above the white rectangle (maybe due to a change of the heat transfer coefficient at the bottom, and thus of the isotherm velocity, probably induced by thermal stresses and air gap formation).

What is really interesting is that out of 12 DS specimens of Al-20 wt pct Zn-0.1 wt pct Cr solidified under identical conditions, 11 exhibited twins, while without chromium, only one had twinned dendrites out of 10 specimens.[38] This clearly demonstrates that Cr, even at very low concentration, favors twinned dendrites formation. While the detailed mechanism is still to be investigated, it is conjectured that the ISRO-induced stacking fault induced by Cr leads to the formation of those twins, as schematically shown in Figure 1. It is also conjectured that in technical aluminum alloys, ISRO- or iQC-inducers such as Cr, Mn or Fe, which are very often present at concentrations of a few hundreds ppm, are most likely responsible of feathery grains formation.

The ISRO-induced stacking fault mechanism, suspected to be responsible for a change of dendrite growth direction and for the formation of twinned grains in Figure 12, is further supported by the results shown in Figure 13. An Al-4.3 wt pct Cu-0.3 wt pct Mg was cast by Henry *et al.*[46] in a DS device similar to that used for the alloy shown in Figure 12. EBSD measurements were made by these authors in various cross sections taken at different distances from the chill plate (Figure 13
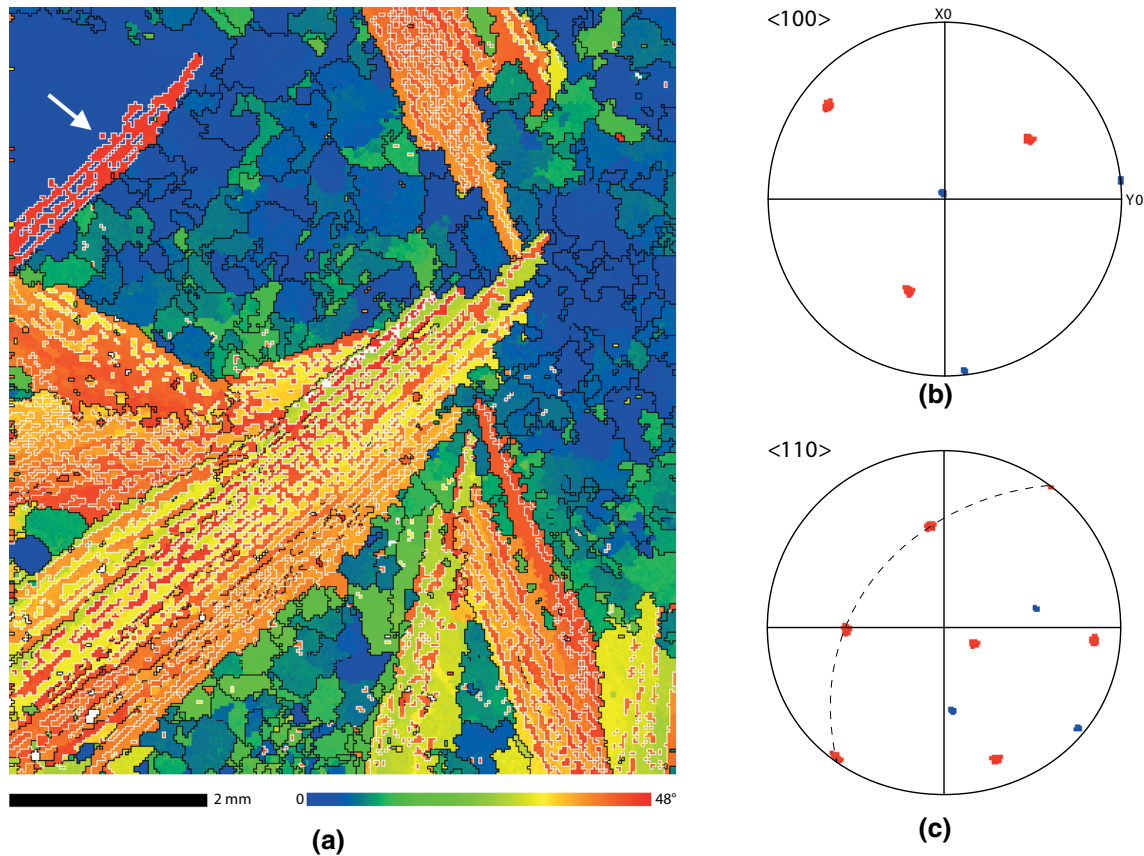
Fig. 13—(*a*) EBSD false color map of a transverse section of an Al-4.3 wt pct Cu-0.3 wt pct Mg directionally solidified sample, taken 6 mm from the chill surface (redrawn from data coming from Ref. [46]). The color of the grains correspond to the angle between the thermal gradient direction (normal to the figure) and the closest ⟨100⟩ direction. Regular dendritic ⟨100⟩ grains appear as small blue or green regions. On the larger blue grain at the top-left corner, red lamellae have formed (arrow). As shown in the corresponding ⟨100⟩ pole figure (*b*), the blue grain has one ⟨100⟩ direction at the center, while the red lamellae are in a twin relationship with the blue grain as indicated in the ⟨110⟩ pole figure (*c*). The common {111} plane is shown with a dashed circle.

corresponds to the section at 6 mm from the chill). In their original work, Henry *et al.* have colored their EBSD microstructure according to the angle between the thermal direction (perpendicular to Figure 13) and the closest ⟨100⟩ or ⟨110⟩ direction.[46] But if they gave the corresponding pole figures for the whole map, they unfortunately did not identify the crystallographic orientation of specific grains.

We have reproduced in Figure 13(a) the EBSD map reconstructed with a color index corresponding to the angle between the closest ⟨100⟩ direction and the thermal gradient. In this section, there is still a majority of regular ⟨100⟩ dendritic grains (blue and green patches), as already pointed out in Reference [46]. These grains have been selected by the growth competition expected for regular dendrites growing along ⟨100⟩. There is a large blue grain at the top left corner of the microstructure (indicated with an arrow), and its corresponding ⟨100⟩ pole figure in (b) clearly shows that it is indeed oriented with a ⟨100⟩ direction parallel to the thermal gradient (normal to the figure). But as can be seen, red lamellae have formed, with blue islands remaining in between. These lamellae are in a twin relationship with the blue grain, as indicated by the ⟨110⟩ pole figure shown in (c). The common {111} twin

plane is indicated with a dashed circle. This situation can be understood with the twin relationship shown in Figure 1(b): a tetrahedron of an ISRO cluster has attached to the blue grain underneath forming a stacking fault (plane 2-3-4 in Figure 1(b)), which then grew as a twin. In other words, the blue grain has acted as a "parent" grain for the formation of twinned lamellae via an ISRO-induced stacking fault mechanism. Unfortunately, Henry *et al.*[46] did not give indication of the purity of their alloy, but it is most likely a technical alloy containing some Fe traces, iron being known like Cr and Mn to form quasicrystals with Al.[18]

The other feathery grains visible in Figure 13(a) appear as yellow, orange or red lamellae: we have verified that they all have a common ⟨110⟩ direction and a common {111} plane nearly parallel to the thermal gradient. For such grains, the formation of the common coherent twin plane can still be explained with the stacking fault mechanism of Figure 1(b). Consider, like for the previous twinned grain, that one tetrahedron of an ISRO cluster attaches to the {111} plane of the fcc parent grain. The stacking fault plane 2-3-4 in Figure 1(b) that we mention for the previous grain is not really favored during growth, since the ⟨110⟩

directions in this plane make an angle of either 90 or 45 deg with respect to the thermal gradient direction (considered to be aligned along ⟨100⟩ of the parent grain). As a matter of fact, the twinned grain labeled with an arrow in Figure 13 has been eliminated and is no longer present in a section taken at 11 mm from the chill (see Figures 5 and 6 in Reference [46]): it has been overgrown, together with regular ⟨100⟩ grains, by twinned grains with a ⟨110⟩ direction nearly aligned with the thermal gradient. If we now consider the other planes of one tetrahedron associated with an ISRO cluster, *e.g.,* plane 1-3-4 in Figure 1(b), they are at 15.8 deg and contain a ⟨110⟩ direction at 19.5 deg from a ⟨100⟩ direction of the parent grain. In other words, twinned grains can form from parent ⟨100⟩ regular dendritric grains if we consider that: (i) ISRO clusters attach with one facet corresponding to {111} planes of the parent grains; (ii) twins emerge from one of the multiple potential pseudo-twins of the icosahedron, the selection being made by its proximity with the thermal gradient direction. Although this is not a proof, it is interesting to observe that most of the twinned grains in Figure 12 are inclined in this longitudinal section with respect to the vertical thermal gradient.

VII. CONCLUSION

Trace elements in metallic alloys, with composition in the range 10 to 1000 ppm, can have a dramatic effect on their solidification behavior, if they induce icosahedral short-range ordering (ISRO) of atoms in the liquid leading to medium-range ordering (IMRO) as the undercooling increases. Such trace elements can be identified from their ability to form quasicrystals with the solvent and other solute elements of these alloys, at least for Al-Cr and Au-Al-Yb. For Au-Ag-Cu alloys with Ir, no quasicrystal has been identified so far but ISRO manifests itself through similar mechanisms.

The first mechanism is ISRO- or iQC-mediated nucleation, in which the fcc phase forms with heteroepitaxy relationships with the icosahedron. This has been clearly identified by multiple twin relationships that exist among nearest-neighbor fcc grains, which are totally compatible with the symmetry of the icosahedron (or interlocked icosahedron [26,29]). The second mechanism is ISRO-induced stacking fault, in which icosahedral clusters attach during growth to the growing fcc phase. This is presently less clear, but the change of dendrite growth direction induced by these trace elements, function of the velocity of the front, the formation of twinned dendrites, the alternated sequence of twinned grains around a central fcc grain, are as many observations which tend to support this conjecture when ISRO-inducers are added.

ISRO also slows down diffusion, as shown by experiments and ab initio calculations. At moderate solidification speed (cm/s), it can induce out-of-equilibrium effects such as a spinodal decomposition with the appearance of new phases.[37] This range of velocity is typical of additive manufacturing and that should be taken into account when developing new alloys for this technology.

It is realized that this new axis of research in the field of solidification, namely the influence of ISRO clusters in the liquid on nucleation, diffusion and attachment kinetics, needs to be consolidated using various experimental techniques in parallel to atomistic calculations: in-situ small-angle scattering of alloys with/without these trace elements, detailed analyses combining 3D FIB-EBSD observations near an iQC-mediated center of nucleation and near the starting point of a twinned grain, diffusion coefficient measurements, longer-range orientation imaging correlation (*i.e,* beyond nearest neighbors), rapid solidification experiments… But it is hoped that this paper will contribute to attract more researchers in this area.

REFERENCES

1. W. Kurz and D.J. Fisher: *Fundamentals of solidification*, Trans. Tech. Publ. Ltd, 4th ed., 1998, Switzerland.
2. J.A. Dantzig and M. Rappaz: *Solidification*, EPFL Press, Presses Polytechniques et Universitaires Romandes, 2nd ed., 2016, Switzerland.
3. C. Herring: *The Physics of Powder Metallurgy*, McGraw-Hill, W.E. Kingston, New York, 1951, pp. 143–79.
4. S. Liu, R.E. Napolitano, and R. Trivedi: *Acta Mater.*, 2001, vol. 49 (20), pp. 4271–76.
5. F. Gonzales and M. Rappaz: *Met. Mater. Trans. A*, 2006, vol. 37 (9), pp. 2797–2806.
6. M. Becker, J.A. Dantzig, M. Kolbe, S.T. Wiese, and F. Kargl: *Acta Mater.*, 2019, vol. 165, pp. 666–77.
7. F. Frank: *Proc. Roy. Soc. Lond. Ser. Math. Phys. Sci.*, 1952, vol. 215 (1120), pp. 43–46.
8. D. Turnbull and J.C. Fisher: *J. Chem. Phys.*, 1949, vol. 17, pp. 71–73.
9. D. Shechtman, I. Blech, D. Gratias, and J.W. Cahn: *Phys. Rev. Lett.*, 1984, vol. 53 (20), pp. 1951–53.
10. M.J. Cooper: *Acta Crystallogr.*, 1960, vol. 13, pp. 257–63.
11. D.W. Deng, Z.M. Mo, and K.H. Kuo: *J. Phys. Condens. Mater.*, 2004, vol. 16, pp. 2283–96.
12. H. Büchler and K.J. Range: *J. Common. Met.*, 1990, vol. 161, pp. 347–54.
13. H. Euchner, M. Mihalkovîc, F. Gähler, M. R. Johnson, H. Schober, S. Rols, E. Suard, A. Bosak, S. Ohhashi, A.-P. Tsai, S. Lidin, C. Pay Gomez, J. Custers, S. Paschen, and M. de Boissieu: *Phys. Rev. B*, 2011, vol. 83, Article Id 144202.
14. M. Boudard: *J. Alloys Compds.*, 2010, vol. 495, pp. 365–71.
15. D. Holland-Moritz, T. Schenk, V. Simonet, R. Bellissent, P. Convert, and T. Hansen: *J. Alloys Compds.*, 2002, vol. 342, pp. 77–81.
16. A. Pasturel and N. Jakse: *Appl. Phys. Lett.*, 2017, vol. 110, art. id 121902.
17. A. Pasturel and N. Jakse: *J. Chem. Phys.*, 2017, vol. 146, art. id 184502.
18. K.F. Kelton: *Int. Mater. Rev.*, 1993, vol. 38 (3), pp. 105–37.
19. G. Kurtuldu, K.F. Shamlaye, and J.F. Löffler: *Proc. Natl. Acad. Sci. U.S.A.*, 2018, vol. 115 (24), pp. 6123–28.

20. K. Kirihara, T. Nakata, M. Takata, Y. Kubota, E. Nishibori, K. Kimura, and M. Sakata: *Phys. Rev. Lett.*, 2000, vol. 85 (16), pp. 3468–71.
21. M. Döblinger, R. Wittmann, D. Gerthsen, and B. Grushko: *Philos. Mag.*, 2003, vol. 83 (9), pp. 1059–74.
22. A.R. Kortan, H.S. Chen, J.M. Parsey, and L.C. Kimerling: *J. Mater. Sci.*, 1989, vol. 24 (6), pp. 1999–2005.
23. A.I. Goldman and R.F. Kelton: *Rev. Mod. Phys.*, 1993, vol. 65 (1), pp. 213–30.
24. J.H. Xia, G. Sha, Z.G. Chen, X.Z. Liao, H.W. Liu, and S.P. Ringer: *Philos. Mag. Lett.*, 2013, vol. 93 (2), pp. 77–84.
25. T. Boncina and F. Zupanic: *Arch. Met. Mater.*, 2017, vol. 62 (1), pp. 5–9.
26. G. Kurtuldu, Ph. Jarry, and M. Rappaz: *Acta Mater.*, 2013, vol. 61 (19), pp. 7098–7108.
27. S. Ino: *J. Phys. Soc. Jpn.*, 1969, vol. 27 (4), pp. 941–53.
28. G. Kurtuldu: Influence of trace elements on the nucleation and solidification morphologies of fcc alloys and relationship with icosahedral quasicrystal formation. PhD thesis #6057, Ecole Polytechnique Fédérale de Lausanne, 2014.
29. G. Kurtuldu, A. Sicco, and M. Rappaz: *Acta Mater.*, 2014, vol. 70, pp. 240–48.
30. G. Kurtuldu, P. Jessner, and M. Rappaz: *J. Alloys Compds.*, 2015, vol. 621, pp. 283–86.
31. C.J. Essig: *Dental Metallurgy: A Manual for the Use of Dental Students*, 3rd ed., The S.S. White Dental Mfg. Co, Philadelphia, 1893.
32. J. Nielsen and J. Tuccillo: *J. Dent. Res.*, 1966, vol. 45, pp. 964–69.
33. A. Tsai, J. Guo, E. Abe, H. Takakura, and T. Sato: *Nature*, 2000, vol. 408 (6812), pp. 537–38.
34. K. Deguchi, S. Matsukawa, N.K. Sato, T. Hattori, K. Ishida, H. Takakura, and T. Ishimasa: *Nat. Mater.*, 2012, vol. 11 (12), pp. 1013–16.
35. S. Matsukawa, K. Tanaka, M. Nakayama, K. Deguchi, K. Imura, H. Takakura, S. Kashimoto, T. Ishimasa and N. K. Sato: *J. Phys. Soc. Jpn.*, 2014, vol. 83 (3), art. id 034705.
36. L. Favre: "Etude de l'affinage de la microstructure de coulée via adjonction d'éléments d'alliage." Master thesis, Ecole Polytechnique Fédérale de Lausanne, 2018.
37. J. Zollinger, B. Rouat, S.K. Pillai, and M. Rappaz: *Met. Mater. Trans. A*, 2019, vol. 50, pp. 2279–88.
38. G. Kurtuldu, Ph. Jarry, and M. Rappaz: *Met. Mater. Trans. A*, 2019, vol. 51A (1), pp. 279–88.
39. M. Rappaz and G. Kurtuldu: *JOM*, 2015, vol. 67 (8), pp. 1812–20.
40. G. Kurtuldu, P. Jarry, and M. Rappaz: *Acta Mater.*, 2016, vol. 115, pp. 423–33.
41. J. Hérenguel: *Rev. Met. Paris*, 1948, vol. 45, pp. 139–46.
42. S. Henry, P. Jarry, and M. Rappaz: *Met. Mater. Trans.*, 1998, vol. 29 (11), pp. 2807–17.
43. S. Henry, G. Gruen, and M. Rappaz: *Met. Mater. Trans.*, 2004, vol. 35A (8), pp. 2495–2501.
44. M.A. Salgado-Ordorica, J.-L. Desbiolles, and M. Rappaz: *Acta Mater.*, 2011, vol. 59 (13), pp. 5074–84.
45. M.A. Salgado-Ordorica, P. Burdet, M. Cantoni, and M. Rappaz: *Acta Mater.*, 2011, vol. 59 (13), pp. 5085–91.
46. S. Henry, T. Minghetti, and M. Rappaz: *Acta Mater.*, 1998, vol. 46 (18), pp. 6431–43.

Publisher's Note Springer Nature remains neutral with regard to jurisdictional claims in published maps and institutional affiliations.